LETTER

Anisotropies in cortical tension reveal the physical basis of polarizing cortical flows

Mirjam Mayer[1,2], Martin Depken[1,2]†*, Justin S. Bois[1,2]*, Frank Jülicher[2] & Stephan W. Grill[1,2]

Asymmetric cell divisions are essential for the development of multicellular organisms. To proceed, they require an initially symmetric cell to polarize[1]. In *Caenorhabditis elegans* zygotes, anteroposterior polarization is facilitated by a large-scale flow of the actomyosin cortex[2-4], which directs the asymmetry of the first mitotic division. Cortical flows appear in many contexts of development[5], but their underlying forces and physical principles remain poorly understood. How actomyosin contractility and cortical tension interact to generate large-scale flow is unclear. Here we report on the subcellular distribution of cortical tension in the polarizing *C. elegans* zygote, which we determined using position- and direction-sensitive laser ablation. We demonstrate that cortical flow is associated with anisotropies in cortical tension and is not driven by gradients in cortical tension, which contradicts previous proposals[5]. These experiments, in conjunction with a theoretical description of active cortical mechanics, identify two prerequisites for large-scale cortical flow: a gradient in actomyosin contractility to drive flow and a sufficiently large viscosity of the cortex to allow flow to be long-ranged. We thus reveal the physical requirements of large-scale intracellular cortical flow that ensure the efficient polarization of the *C. elegans* zygote.

Understanding polarization of the *C. elegans* zygote requires an understanding of cortical flows and their driving forces. At the onset of polarization, indicators of contractility (myosin foci and membrane ruffles) are uniformly distributed throughout the actomyosin cortex[4]. A centrosome-associated cue disrupts this even distribution by local myosin downregulation near the posterior pole[3,6]. This induces anterior-directed cortical flows, which facilitate the segregation of cell-fate determinants between the anterior and posterior domain[4,7]. Flows are subject to biochemical feedback[4,7-9] and persist for several minutes; they do not resemble a singular elastic relaxation. During polarization the cortex constantly contracts, rearranges and turns over, suggesting that its active and fluid properties are important[10,11].

Two main factors are known to play a role in cortical dynamics: actomyosin contractility and cortical tension. It is important to recognize that they are distinct[12]. Actomyosin contractility (active tension) refers to the forces actively generated by cortical myosin motors. Cortical tension (total mechanical tension) refers to the forces that actually reside in the cortex (Supplementary Table 1). Although cortical tension has recently drawn interest for its function in various stages of animal development[13], its role in flows remains unclear. It has been proposed that gradients in cortical tension constitute the driving force for cortical flow[5], but this has never been tested *in vivo*.

We characterized cortical tension in the polarizing zygote with both positional and directional resolution. To this end, we ablated the actomyosin meshwork with a pulsed ultraviolet laser[14] along a 6-μm line (cortical laser ablation, COLA, Fig. 1a, Supplementary Figs 1 and 2) in embryos expressing green fluorescent protein (GFP)-labelled non-muscle myosin 2 (NMY-2–GFP) (similar results were obtained with the actin marker moesin (GFP–MOE), Supplementary Fig. 3). Following COLA, the adjacent cortex rapidly displaced away orthogonally to the cut line and

continued moving outwards for several seconds (Fig. 1, Supplementary Movie 1) before undergoing wound-healing[15] (Supplementary Fig. 4). Cortical tension is proportional to the initial outward velocity v_0 of the cortex after COLA (Supplementary Section 4.2). The outward velocity decayed exponentially over time (Figs 1c, f and 2), which is characteristic of a simple viscoelastic response[16]. The associated decay time constant τ is a signature of the mechanical properties of the cortex, in particular its stiffness (Supplementary Information Section 2.4). Thus, COLA allows position- and direction-sensitive quantification of cortical tension in living embryos.

We first probed cortical tension in the direction orthogonal to the anteroposterior (AP) axis ('orthogonal cortical tension'), because there are essentially no flows in this direction. We asked whether tension in this direction differs between the myosin-rich anterior and the myosin-depleted posterior domains[17,18]. To measure orthogonal cortical tension, we performed COLA along the AP axis of NMY-2–GFP embryos and followed cortical movements orthogonal to the ablated line. We found a significantly enhanced response in the anterior cortex, compared with that in the posterior cortex (Fig. 1a–f, Supplementary Movies 1 and 2), with an initial orthogonal outward velocity $v_{0,\perp} = 9.15 \pm 0.84\,\mu m$ min^{-1} (all errors are errors of the mean at 95% confidence unless otherwise stated) in the anterior ($n = 120$) and $v_{0,\perp} = 3.81 \pm 0.82\,\mu m\,min^{-1}$ in the posterior domain ($n = 88$). The decay time constant τ differed slightly between the anterior (2.7 ± 0.3 s) and posterior (3.9 ± 0.9 s, Fig. 2b insets), consistent with a stiffer anterior cortex due to higher density of cortical F-actin[19] (Supplementary Fig. 5). Our results demonstrate that orthogonal cortical tension is twice as high in the myosin-rich anterior cortex as in the posterior cortex, where myosin levels are reduced.

We expect orthogonal cortical tension to be high in both domains under conditions in which myosin concentrations remain high throughout the cortex. To test this, we used RNA interference (RNAi) to deplete embryos of spindle defective 5 (SPD-5), a protein required for centrosome maturation and symmetry breaking[20]. Performing COLA along the AP axis, we observed a strong cut response in both domains (Fig. 1g–j, Supplementary Movies 4 and 5), with similar $v_{0,\perp}$ in the anterior ($10.61 \pm 2.03\,\mu m\,min^{-1}$, $n = 26$) and posterior cortex ($8.61 \pm 2.40\,\mu m$ min^{-1}, $n = 23$). Hence, orthogonal cortical tension does not differ significantly within the cortex under *spd-5*(RNAi).

We next investigated how cortical tension is biochemically regulated. Using RNAi against two antagonistic regulators of the small G protein RHO-1, the GTPase activating protein (GAP) RGA-3 (refs 21, 22), and the guanine nucleotide exchange factor (GEF) ECT-2 (ref. 8), we tested for regulation of cortical tension by means of the Rho-GTPase cycle[23]. We conducted anterior COLA along the AP axis in zygotes that were globally depleted of either the GAP or the GEF, but still polarized. *Ect-2(RNAi)* embryos displayed a weak recoil ($v_{0,\perp} = 3.76 \pm 1.62\,\mu m\,min^{-1}$, $n = 16$; Fig. 3, Supplementary Movie 6), similar to posterior COLA in non-RNAi embryos. Conversely, we observed a vigorous COLA response in *rga-3(RNAi)* embryos ($v_{0,\perp} = 11.39 \pm 1.75\,\mu m$ min^{-1}, $n = 35$; Fig. 3, Supplementary Movie 7), with $v_{0,\perp}$ exceeding anterior velocities of

[1]Max Planck Institute of Molecular Cell Biology and Genetics, 01307 Dresden, Germany. [2]Max Planck Institute for the Physics of Complex Systems, 01187 Dresden, Germany. †Present address: Vrije Universiteit Amsterdam, 1081 HV Amsterdam, The Netherlands.
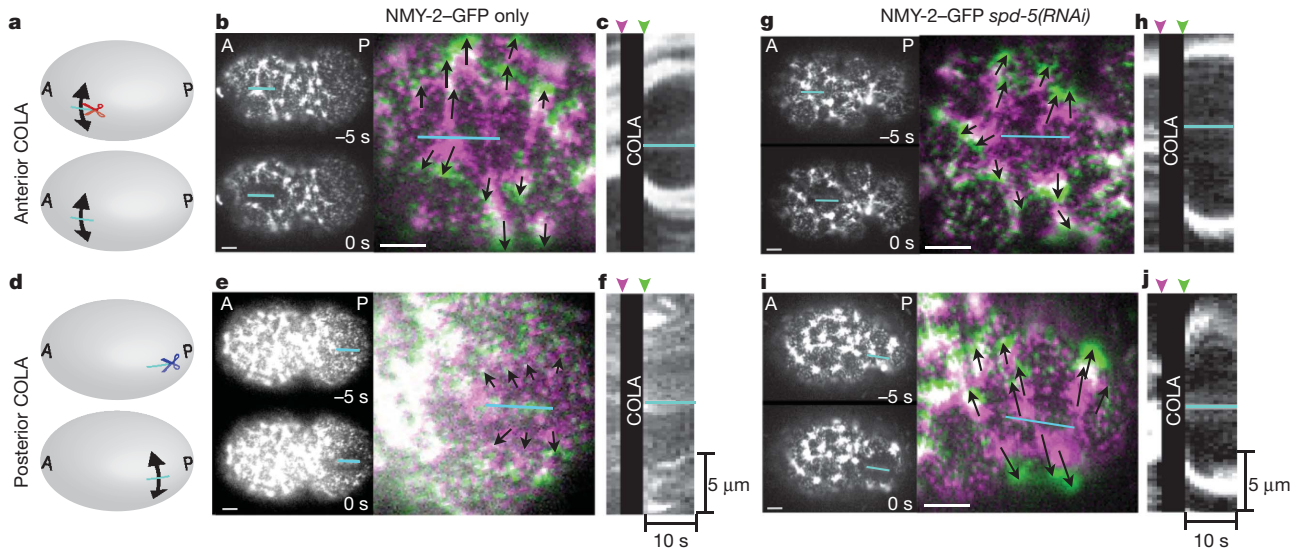*These authors contributed equally to this work.

Figure 1 | Orthogonal cortical tension in the anterior and posterior domain of *C. elegans* zygotes measured by COLA. a, Schematic of anterior COLA along the AP axis. COLA (scissors) was performed along a 6-μm line (light blue). Black arrows, cortical recoil after COLA. A, anterior; P, posterior. **b**, Pre-(top left) and post-cut image (bottom left) of anterior COLA in an NMY-2–GFP zygote. Right, enlarged overlay. Arrows, displacements between pre-cut (purple) and post-cut frame (green). **c**, Kymograph (representation of spatial position over time) recorded perpendicular to the cut line. Arrowheads mark pre- and post-cut frames, separated by 5 s COLA. **d–f**, Posterior COLA with schematic (**d**) and kymograph (**f**). **g, h**, Anterior COLA in SPD-5-depleted NMY-2–GFP zygotes with kymographs. **i, j**, Posterior COLA in SPD-5-depleted NMY-2–GFP zygotes with kymographs. Scale bars, 5 μm.

non-RNAi embryos. We conclude that reducing RGA-3 upregulates orthogonal tension in the anterior cortex, whereas reducing ECT-2 downregulates it.

We have so far investigated cortical tension orthogonal to flow, where the force balance in the cortex is simple: contractility and cortical

tension are equal because all contractile forces generate cortical tension. In the presence of flow, the force balance is more complicated because viscous stresses arise due to movement and deformation of the flowing cortex. Therefore, cortical tension could be affected by flow and differ between the directions along and across the AP axis. We measured
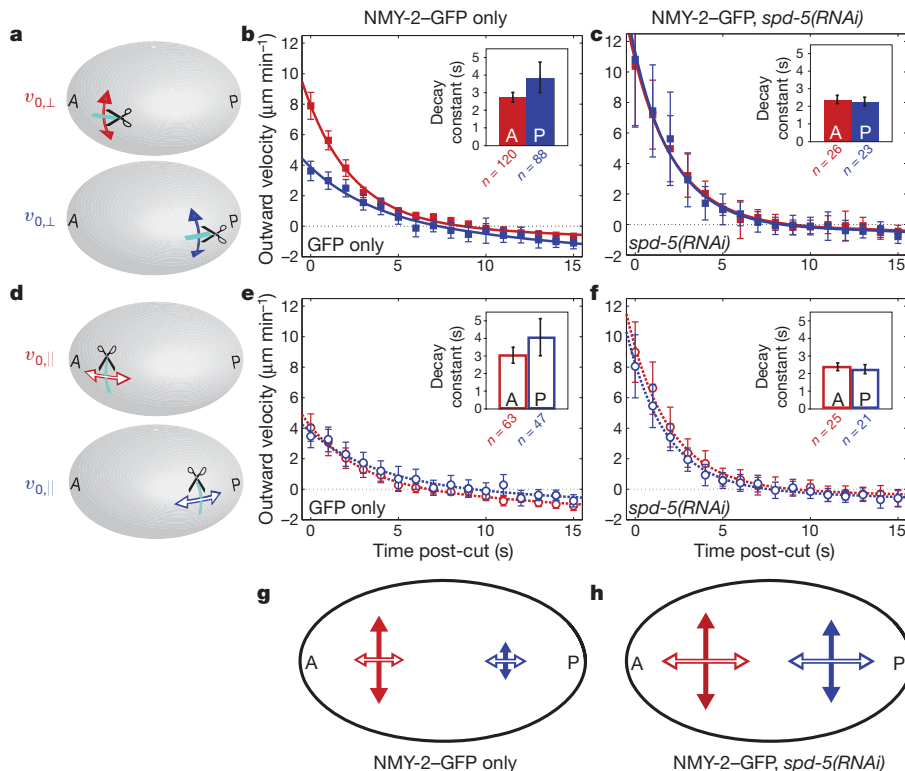

Figure 2 | COLA response. a, Schematic of COLA along the AP axis (light blue); red (top, anterior) and dark-blue (bottom, posterior) arrows indicate displacements. A, anterior; P, posterior. **b, c**, Orthogonal anterior (red) and posterior (dark-blue) outward velocities as a function of time for GFP-only (**b**) and *spd-5(RNAi)* (**c**) zygotes. Decays are fitted by the sum of a single exponential and linear decay function (see Methods). Insets, decay time constants τ. **d–f**, COLA orthogonal to the AP axis. Parallel outward velocities as a function of time for GFP-only (**e**) and *spd-5(RNAi)* (**f**) zygotes. **g, h**, Distribution of cortical tension in non-RNAi embryos (**g**) during flows and *spd-5(RNAi)*-embryos (**h**) without flow; arrow lengths proportional to $v_{0,\perp}$ in the orthogonal (closed symbols) and $v_{0,\parallel}$ in the parallel (open symbols) direction. Note that we also observe anisotropies when analysing the spatial dependence of rupture events between myosin foci (Supplementary Fig. 7). Error bars, error of the mean at 95% confidence.
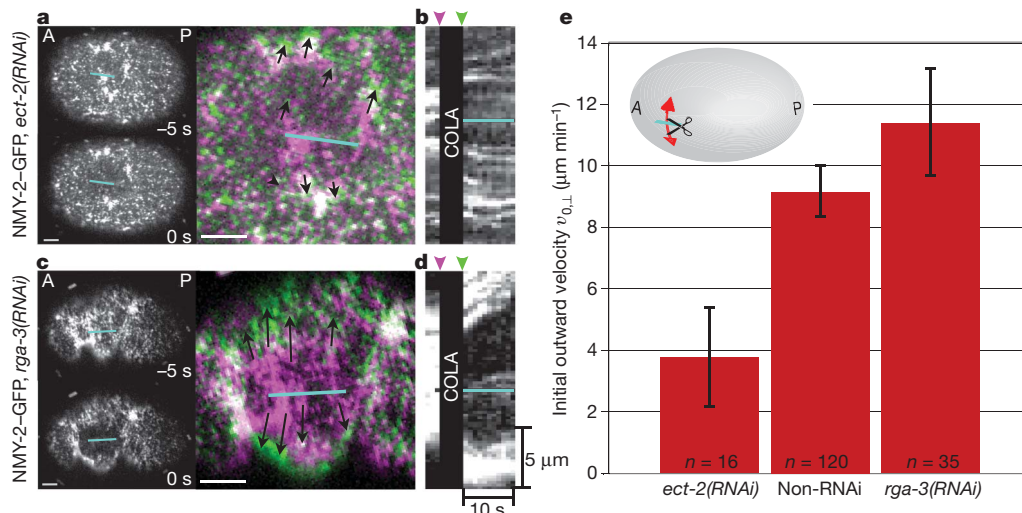
Figure 3 | Orthogonal cortical tension is under control of the Rho-GTPase cycle. a, Pre- (top left) and post-cut image (bottom left) of anterior COLA along the AP axis (light blue) in NMY-2–GFP *ect-2(RNAi)* zygotes. Right, enlarged overlay. Arrows, displacements between pre-cut (purple) and post-cut (green) frames. **b**, Kymograph recorded perpendicular to the cut. Arrowheads mark pre- and post-cut frames. **c**, Anterior COLA along the AP axis with **d**, kymograph in NMY-2–GFP *rga-3(RNAi)*. **e**, Corresponding anterior $v_{0,\perp}$ in *ect-2(RNAi)*, non-RNAi and *rga-3(RNAi)* embryos. Inset, COLA schematic. Scale bars, 5 μm. Error bars, error of the mean at 95% confidence.

anterior cortical tension along the AP axis ('parallel cortical tension') by performing COLA along a 6-μm line orthogonal to the AP axis (Supplementary Movie 8). The reaction we observed in this direction was significantly weaker (initial parallel outward velocity, $v_{0,||} = 4.97 \pm 0.93\,\mu\text{m min}^{-1}$, $n = 63$) than the orthogonal response measured in this domain (see above; Fig. 2b, e, g). This demonstrates a marked anisotropy of cortical tension in the anterior, with parallel cortical tension significantly smaller than orthogonal cortical tension.

To verify that the observed anisotropy is a direct result of flow, we tested whether cortical tension is isotropic in polarization-deficient embryos in which anterior-directed flows are absent. We found that cortical tension was isotropic and high in both domains of *spd-5(RNAi)* embryos (anterior: $v_{0,\perp} = 10.16 \pm 2.03\,\mu\text{m min}^{-1}$, $n = 26$; $v_{0,||} = 8.76 \pm 1.43\,\mu\text{m min}^{-1}$, $n = 25$; posterior: $v_{0,\perp} = 8.61 \pm 2.40\,\mu\text{m min}^{-1}$, $n = 23$; $v_{0,||} = 8.86 \pm 1.78\,\mu\text{m min}^{-1}$, $n = 21$; Fig. 2c, f, h; Supplementary Movies 4, 5, 9 and 10) and similar to anterior orthogonal tension during flows (Fig. 2). Consistent with this, cortical tension was also isotropic (albeit reduced overall) in non-RNAi embryos before flow onset (Supplementary Fig. 8). Furthermore, the decay time constant τ in the anterior during flows did not differ significantly between the two directions, and was similar to that measured in both domains and both directions when flow was inhibited by depleting SPD-5 (insets Fig. 2b,c,f). This suggests that the mechanical properties of the cortex are isotropic and that anisotropies in cortical tension are a direct consequence of flows.

To understand how cortical flow generates these anisotropies, we investigated the cortical force balance. We first analysed AP profiles of flow velocity and myosin density. The myosin density distribution (serving as a measure of contractility) is uniformly high in the anterior and decreases towards the posterior pole[4]. Anterior-directed flows reach their highest velocity within the posterior domain and slow down towards the anterior before ceasing near the anterior pole (Fig. 4a, b, Supplementary Movie 11). This velocity decrease implies that the cortex is not only moving towards the anterior, but is compressed at the same time. Translocation and deformation are subject to distinct dissipative effects: translocation is resisted by friction between the cortex and the cytoplasm/membrane/eggshell; deformation is resisted by internal viscosity on long time scales, because the actomyosin meshwork requires remodelling during compression (Fig. 4c, d). Furthermore, we measured a time constant of 28.7 ± 2.2 s for cortical myosin turnover ($n = 11$, Supplementary Fig. 10a), suggesting that

elastic contributions to the force balance can be neglected when considering time scales longer than this turnover time[24,25]. To quantify the force balance, we next developed a physical description that treats the cortex as a thin film of active viscous fluid[10,26,27]. Here, cortical tension T along a given direction x is not only the result of contractility (active tension) C, but also depends on the effective viscosity η within the cortex and the local rate of compression $\partial v/\partial x$, where v describes the flow velocity along the x-axis (Supplementary Section 4.3): $T = C + \eta\,\partial v/\partial x$. Additionally, friction affects the tension gradient according to $\partial T/\partial x = \gamma\,v$, where γ is a friction coefficient. This thin-film active fluid description is valid for timescales that are large compared to cortical turnover time, and for length scales that are large compared to local inhomogeneities (myosin foci; Supplementary Fig. 6).

We next asked whether friction or viscosity dominates. If the cortex can be rapidly compressed or expanded, cortical viscosity can be neglected ($\eta \approx 0$). Cortical tension is then unaffected by flow, directly determined by contractility, and isotropic. Conversely, if the cortex can be easily moved relative to its environment, friction can be neglected ($\gamma \approx 0$). Parallel cortical tension is then constant, and no cortical tension gradient exists along the AP axis even in the presence of flow ($\partial T/\partial x \approx 0$). Our experiments revealed that cortical tension is anisotropic, demonstrating that cortical viscosity cannot be neglected. To determine whether friction can be neglected, we tested for the existence of an AP cortical tension gradient by measuring parallel tension in the posterior cortex (Supplementary Movie 12). We found that the response ($v_{0,||} = 4.29 \pm 1.06\,\mu\text{m min}^{-1}$, $n = 47$) was not significantly different from anterior $v_{0,||}$ (Fig. 2). This demonstrates that there is no detectable AP gradient in cortical tension and implies that external friction can be neglected. Our finding is in contrast to previous considerations, which postulated cortical tension gradients as a driving force for cortical flows[5].

Why is cortical flow associated with anisotropies in cortical tension, but not with tension gradients? We have demonstrated that this is because viscosity dominates over friction, and now argue that there is a physiological reason for this. If friction were to dominate over viscosity, a local contraction would result in the localized expansion of adjacent material, without affecting the cortex further away. Only a sufficiently viscous cortex supports a long-ranged flow towards a contracting region (Fig. 4e, Supplementary Movie 13). Our theoretical description reveals a hydrodynamic length scale $\ell = (\eta/\gamma)^{1/2}$ (Supplementary Section 4.3), which describes the extent to which the flow
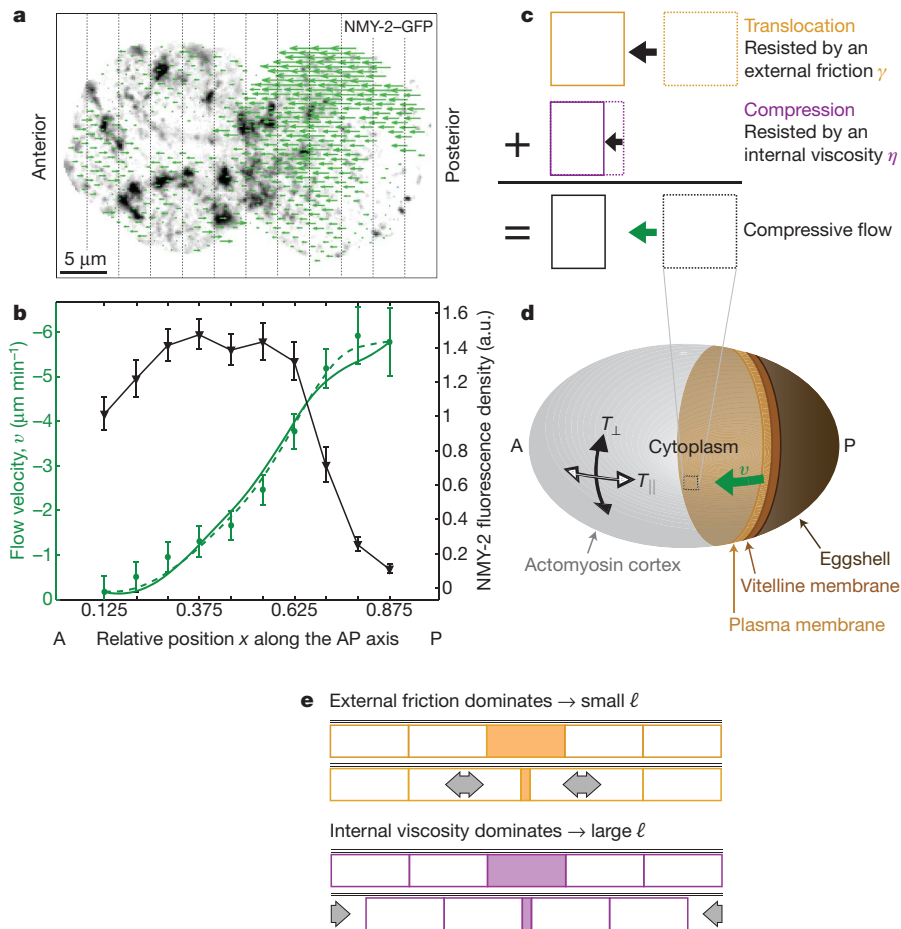
Figure 4 | Flow and density profiles demonstrate long-ranged flow.
a, NMY-2–GFP at 30% retraction with PIV flow field; AP velocity proportional to length of arrows. **b**, Averaged NMY-2 density (black triangles) and cortical flow velocity (green circles) as functions of position along the AP axis. $n = 75$ embryos; error bars, error of the mean at 95% confidence. Green curves, theoretical velocity profiles, with contractility directly proportional to the measured NMY-2 density (solid curve, $\ell = 0.30$ AP length) and for saturation (dashed curve, $\ell = 0.27$ AP length, Supplementary Information Section 4.3). **c**, Cortical flow can be decomposed into translocation (anterior movement) and deformation (compression). **d**, Sketch of the flowing embryo cortex (grey) moving with respect to the cytoplasm and outer layers; $T_{\parallel}$, parallel cortical tension; $T_{\perp}$, orthogonal cortical tension. Green arrow, anterior-directed flow. **e**, Internal viscosity and external friction set a hydrodynamic length scale $\ell = (\eta/\gamma)^{1/2}$. If friction dominates (top), local contraction (shaded box) only results in the expansion of adjacent material. To achieve long-ranged flow (bottom), viscosity must dominate over friction (Supplementary Movie 13).

is long-ranged. We determined ℓ by calculating the theoretical flow profile from the experimental myosin distribution (Fig. 4b). The calculated profile best matches the experimentally measured one for $\ell \approx 14\,\mu m$, demonstrating that localized contractions can move the cortex over a significant fraction of the length of the embryo. We propose that the existence of anisotropies in cortical tension and the absence of tension gradients result from the biological necessity of contractile flow to be long-ranged, suggesting that cortical properties are tuned to enable long-ranged flow for robust AP polarization.

Finally, we tested whether changes in the turnover and activity of cortical components affect cortical viscosity[24,25]. Mild depletion of the actin depolymerizing/severing factor cofilin (UNC-60) or the myosin regulatory light chain (MLC-4) increased the NMY-2–GFP turnover time approximately 2.5-fold. We observed that it also increased the hydrodynamic length scale to more than 25 μm in both cases, consistent with an increased viscosity (Supplementary Fig. 10). Conversely, we found that treatment with the actin polymerization inhibitor cytochalasin D induced a period of short-ranged flow (Supplementary Fig. 11, Supplementary Movie 14), consistent with a reduced viscosity due to actin meshwork disassembly, before flows were lost entirely[28]. These results illustrate that the emergence of cortical viscosity is closely related to the activity and turnover of cortical components, and it might be interesting to investigate whether cortical viscosity itself is subject to spatio-temporal regulation[29].

By mapping cortical tension through location- and direction-sensitive COLA measurements, we have unveiled the physical mechanisms of cortical flow in *C. elegans*. Many developmental rearrangements both at the single-cell level and in multicellular tissues rely on tension and flow[5,30], and it will be interesting to see whether they are governed by similar physical principles.

METHODS SUMMARY

Culture conditions, strains and gene silencing by RNAi. Worm strains, handling and RNAi conditions used in this study are detailed in the Supplementary Methods.
COLA. We conducted cortical laser ablation using methods similar to those in ref. 14. We performed COLA at 30% retraction by applying 50 ultraviolet pulses at 500 Hz to five equidistant sites along a 6-μm line. We analysed the initial outward velocity v_0 after COLA using particle image velocimetry (PIV).
PIV. We determined the initial outward velocity v_0 after COLA and the overall flow fields of polarizing embryos with a custom-made PIV algorithm (detailed in the Supplementary Methods) using Matlab (Mathworks) and implementing Gaussian fitting to achieve subpixel resolution.

Full Methods and any associated references are available in the online version of the paper at www.nature.com/nature.

1. Horvitz, H. R. & Herskowitz, I. Mechanisms of asymmetric cell division: two Bs or not two Bs, that is the question. *Cell* **68,** 237–255 (1992).

2. Hird, S. N. & White, J. G. Cortical and cytoplasmic flow polarity in early embryonic cells of *Caenorhabditis elegans*. *J. Cell Biol.* **121,** 1343–1355 (1993).
3. Goldstein, B. & Hird, S. N. Specification of the anteroposterior axis in *Caenorhabditis elegans*. *Development* **122,** 1467–1474 (1996).
4. Munro, E., Nance, J. & Priess, J. R. Cortical flows powered by asymmetrical contraction transport PAR proteins to establish and maintain anterior-posterior polarity in the early *C. elegans* embryo. *Dev. Cell* **7,** 413–424 (2004).
5. Bray, D. & White, J. G. Cortical flow in animal cells. *Science* **239,** 883–888 (1988).
6. Cowan, C. R. & Hyman, A. A. Centrosomes direct cell polarity independently of microtubule assembly in *C. elegans* embryos. *Nature* **431,** 92–96 (2004).
7. Cheeks, R. J. *et al. elegans* PAR proteins function by mobilizing and stabilizing asymmetrically localized protein complexes. *Curr. Biol.* **14,** 851–862 (2004).
8. Motegi, F. & Sugimoto, A. Sequential functioning of the ECT-2 RhoGEF, RHO-1 and CDC-42 establishes cell polarity in *Caenorhabditis elegans* embryos. *Nature Cell Biol.* **8,** 978–985 (2006).
9. Zonies, S., Motegi, F., Hao, Y. & Seydoux, G. Symmetry breaking and polarization of the *C. elegans* zygote by the polarity protein PAR-2. *Development* **137,** 1669–1677 (2010).
10. Kruse, K., Joanny, J.-F., Jülicher, F., Prost, J. & Sekimoto, K. Generic theory of active polar gels: a paradigm for cytoskeletal dynamics. *Eur. Phys. J. E* **16,** 5–16 (2005).
11. Munro, E. M. & Bowerman, B. Cellular symmetry breaking during *Caenorhabditis elegans* development. *Cold Spring Harb. Perspect. Biol.* **1,** a003400 (2009).
12. Wozniak, M. A. & Chen, C. S. Mechanotransduction in development: a growing role for contractility. *Nature Rev. Mol. Cell Biol.* **10,** 34–43 (2009).
13. Lecuit, T. & Lenne, P.-F. Cell surface mechanics and the control of cell shape, tissue patterns and morphogenesis. *Nature Rev. Mol. Cell Biol.* **8,** 633–644 (2007).
14. Grill, S. W., Gönczy, P., Stelzer, E. & Hyman, A. A. Polarity controls forces governing asymmetric spindle positioning in the *Caenorhabditis elegans* embryo. *Nature* **409,** 630–633 (2001).
15. Mandato, C. A. & Bement, W. M. Contraction and polymerization cooperate to assemble and close actomyosin rings around *Xenopus* oocyte wounds. *J. Cell Biol.* **154,** 785–797 (2001).
16. Wottawah, F. *et al.* Optical rheology of biological cells. *Phys. Rev. Lett.* **94,** 098103 (2005).
17. Dai, J., Ting-Beall, H. P., Hochmuth, R. M., Sheetz, M. & Titus, M. A. Myosin I contributes to the generation of resting cortical tension. *Biophys. J.* **77,** 1168–1176 (1999).
18. Pasternak, C., Spudich, J. A. & Elson, E. L. Capping of surface receptors and concomitant cortical tension are generated by conventional myosin. *Nature* **341,** 549–551 (1989).
19. Strome, S. Fluorescence visualization of the distribution of microfilaments in gonads and early embryos of the nematode *Caenorhabditis elegans*. *J. Cell Biol.* **103,** 2241–2252 (1986).
20. Hamill, D. R., Severson, A. F., Carter, J. C. & Bowerman, B. Centrosome maturation and mitotic spindle assembly in *C. elegans* require SPD-5, a protein with multiple coiled-coil domains. *Dev. Cell* **3,** 673–684 (2002).
21. Schonegg, S., Constantinescu, A. T., Hoege, C. & Hyman, A. A. The Rho GTPase-activating proteins RGA-3 and RGA-4 are required to set the initial size of PAR domains in *Caenorhabditis elegans* one-cell embryos. *Proc. Natl Acad. Sci. USA* **104,** 14976–14981 (2007).
22. Schmutz, C., Stevens, J. & Spang, A. Functions of the novel RhoGAP proteins RGA-3 and RGA-4 in the germ line and in the early embryo of *C. elegans*. *Development* **134,** 3495–3505 (2007).
23. Glotzer, M. The molecular requirements for cytokinesis. *Science* **307,** 1735–1739 (2005).
24. Humphrey, D., Duggan, C., Saha, D., Smith, D. & Käs, J. Active fluidization of polymer networks through molecular motors. *Nature* **416,** 413–416 (2002).
25. Lieleg, O., Claessens, M. M. A. E., Luan, Y. & Bausch, A. R. Transient binding and dissipation in cross-linked actin networks. *Phys. Rev. Lett.* **101,** 108101 (2008).
26. Aditi Simha, R. & Ramaswamy, S. Hydrodynamic fluctuations and instabilities in ordered suspensions of self-propelled particles. *Phys. Rev. Lett.* **89,** 058101 (2002).
27. Salbreux, G., Prost, J. & Joanny, J.-F. Hydrodynamics of cellular cortical flows and the formation of contractile rings. *Phys. Rev. Lett.* **103,** 058102 (2009).
28. Strome, S. & Wood, W. B. Generation of asymmetry and segregation of germ-line granules in early *C. elegans* embryos. *Cell* **35,** 15–25 (1983).
29. Zhang, W. & Robinson, D. N. Balance of actively generated contractile and resistive forces controls cytokinesis dynamics. *Proc. Natl Acad. Sci. USA* **102,** 7186–7191 (2005).
30. Rauzi, M., Verant, P., Lecuit, T. & Lenne, P.-F. Nature and anisotropy of cortical forces orienting *Drosophila* tissue morphogenesis. *Nature Cell Biol.* **10,** 1401–1410 (2008).

METHODS

Culture conditions, strains and sample preparation. We cultured and handled *C. elegans* embryos as described[31]. We used transgenic strains JJ1473 (NMY-2–GFP; ref. 32) and nnIs (unc-119(+) GFP–Dm-MOE(437-578); ref. 33), both of which are under the control of the *pie-1* promoter. We grew strains at 20 °C and imaged them at 22–24 °C. We dissected worms in 0.1 M NaCl/4% sucrose and mounted embryos on agar pads (2% agarose in 0.1 M NaCl/4% sucrose). We slightly compressed embryos between the agarose pad and a coverslip to increase the cortical surface visible in a confocal plane.

Gene silencing by RNAi. We performed RNAi experiments by feeding as described[34,35] and incubated worms for 14–36 h at 25 °C on feeding plates (nematode growth medium agar containing 0.5–2.0 mM isopropyl-β-D-thiogalactoside and 25 μg ml⁻¹ carbenicillin) before analysing their progeny. With the exception of *mlc-4*, which was provided by Nate Goehring, and *unc-60*, which was a gift from Carrie Cowan, we obtained the feeding clones used from Geneservice (http://www.geneservice.co.uk).

The feeding clones contained the respective target sequence amplified with the following primers and cloned into the RNAi feeding vector L4440, which was transformed into HT115 bacteria[35].

rga-3: K09H11.3 GCAAGGAAGGCAACTCTGTCGTTATTTCTCGGTGTGGCGT

ect-2: T19E10.1 CTCTGATTTCTGCCAAAGCCGGCAAAGAAATCCGATTCA

spd-5: F56A3.4 CTTTCTCTGGGAAGAATGCGTTTTCGTCTGCTGATGTTCG

unc-60: C38C3.5a TTGGATCCATGAGTTCCGGTGTCATGGT CCGCGGCCG CTAGTGATCTCCGTATTTCT

For the *mlc-4* feeding clone the entire genomic sequence (C56G7.1) was subcloned using the Gateway system into L4440GW, a Gateway derivative of the L4440 feeding vector, and also transformed into HT115 bacteria.

COLA. We conducted laser ablation on a previously described set-up[14]. We performed COLA at 30% retraction (that is, when the anterior myosin-rich cortex occupied 70% and the posterior cortex 30% of the embryo length), or the equivalent stage in the cell cycle, by applying 50 ultraviolet pulses at 500 Hz to five equidistant sites along a 6-μm line. This length was a compromise between averaging over local inhomogeneities (myosin foci, 4.8 μm average inter-foci distance; Supplementary Fig. 6) and keeping the extent of the perturbation small compared to the size of the embryo. We acquired fluorescent images with an ORCA ER camera using 2 × 2 binning, and integration times of 150–300 ms. (We exposed posterior COLA experiments and *ect-2(RNAi)* zygotes for longer because they had reduced fluorescence intensities owing to NMY-2 downregulation.) The frame rate was 1 s before and after COLA; COLA itself had a duration of 5 s, during which no images were acquired (Supplementary Fig. 1a).

PIV. We quantified cortical velocity both for COLA and for cortical flow measurements using PIV[36,37]. Our algorithm is based on the cross-correlation of a pair of subsequent images (using Matlab's built-in function normxcorr2), quantifying movements on the basis of the largest similarity between templates in the first frame and their respective counterparts in the subsequent frame. PIV does not depend on the presence of particles of defined shapes or sizes. This allows for an automated, unbiased calculation of velocity fields in both the anterior and posterior of non-RNAi embryos and under different RNAi conditions, in which the particles (NMY-2 foci and puncta) had different features. Our algorithm implemented Gaussian fitting to achieve subpixel resolution. Before data analysis, we tested different PIV parameters for computing velocity profiles of cortical flows and post-COLA responses. These gave comparable results, demonstrating robust quantification by PIV with the use of one defined set of parameters for all analyses.

Quantification of v_0 and τ after COLA. The physical properties of interest in a COLA experiment are cortical tension and cortical stiffness. As shown in Supplementary Information Section 4.2, cortical tension is proportional to the velocity away from the ablation line immediately after COLA (v_0), and the stiffness is inversely proportional to the decay time constant of the velocity (τ). To determine the initial outward velocity we applied PIV (see above) to the pre- and post-cut frames, yielding the velocity field over the 5-s cut duration. The velocity component orthogonal to the cut line (Supplementary Fig. 1b, black arrows) was averaged in two regions adjacent to the cut (Supplementary Fig. 1b, yellow boxes), yielding the mean initial outward velocity, v_0^{mean}, over the 5-s cut duration.

To assess the temporal cortical recoil after COLA, we determined the outward velocity for post-cut frames up to 15 s after COLA, where the time interval between frames was 1 s, by averaging the orthogonal component of the calculated PIV flow field over the two adjacent areas. The outward velocity decayed over time in each experiment separately. The averaged data for each experimental condition showed similar decay (Supplementary Fig. 1c). Over the first 10 s, the initial velocity decay after COLA was well described by a single exponential decay, consistent with known viscoelastic properties of actomyosin cortices[16,38]. For times longer than about 10 s after COLA, the data deviated from the single exponential decay

because of wound healing, in which the outward velocities reversed and assumed negative values (Fig. 2 and Supplementary Fig. 2).

Cortical resealing after COLA appears to be the combination of two processes: an accumulation of central actomyosin at the cut site and an inward-directed movement from the rim of the cut towards its centre (Supplementary Fig. 4). To account for this inward-directed resealing, which results in negative outward velocities for longer times, we incorporated a correction term in the exponential fit functions for the velocity decays after COLA. We assumed this resealing correction term to be linear in time: $v(t) = v_0 e^{-t/\tau} - bt$. A resealing velocity that linearly increases with time might arise from the increasing accumulation of actomyosin at the centre of the cut site[15]. However, it is also possible that wound healing leads to a resealing velocity that is constant in time, resulting in a velocity function of the form $v(t) = v_0 e^{-t/\tau} - d$. In both cases, the individual and the average velocity decays were well fitted (coefficient of determination, $R^2 > 0.98$ for all conditions) and gave consistent results (Supplementary Table 2). Because the associated R^2 values were larger on average for the linear resealing kinetics (Supplementary Table 2), we report these values in the main text.

In addition to determining the decay time constant τ, fitting experimental velocity decays also provides another way to obtain the initial outward velocity after COLA, reported as v_0^{fit} in Supplementary Table 2. Importantly, v_0^{mean} and v_0^{fit} were in very good agreement for all experimental conditions tested (Supplementary Fig. 1d and Supplementary Table 2), verifying that COLA captures the dominant fast relaxation due to tension release. The results reported in the main text as v_0 are velocities obtained by comparing pre- and post-cut images (v_0^{mean}).

The specificity of the cortical response to COLA and the reliability of our PIV algorithm were tested for each experiment in a control by cross-correlating two frames of 5-s interval before COLA as described above. Because no laser ablation had occurred, these controls did not show any directed movement in the two regions averaged for analysis, resulting in outward velocities that were not significantly different from zero (Supplementary Fig. 1b, left panel, and Supplementary Fig. 1d). These controls confirm that the initial outward velocities after COLA result from the laser ablation and are adequately captured by PIV.

The velocity decay constant is given by $\tau = \zeta / k$, as described in Supplementary Section 4.2, where k is the elastic stiffness of the cortex and ζ characterizes frictional interactions between the cortex and the entraining fluid. Because the cytosol, and therefore the fluid in which the cortex is embedded, is likely to be uniform throughout the embryo[39,40], differences in τ probably reflect differences in stiffness. A plausible cause for varying τ is a slightly stiffer anterior cortex due to larger densities of F-actin in that region[19,41,42]. To test whether such an explanation is quantitatively consistent with the observed anterior and posterior relaxation constants, we quantified the fluorescence intensity of 24 GFP–MOE-expressing zygotes at the time of 30% retraction in anterior and posterior regions of fixed area (Supplementary Fig. 5a), normalized them by the background fluorescence intensity and calculated the ratio of normalized F-actin density between the anterior and posterior cortex. We found the F-actin density to be on average 1.32 ± 0.16 times higher in the anterior than in the posterior domain. Because τ is inversely proportional to the stiffness of the material, we determined the ratio $\tau_{\text{posterior}}/\tau_{\text{anterior}}$, obtaining the result 1.41 ± 0.50, which was very similar to the ratio of actin densities (Supplementary Fig. 5). Therefore, differences in relaxation times probably represent differences in stiffness, which could simply result from different associated F-actin densities. We note, however, that alternative explanations, such as strain hardening[43,44], are also plausible.

Survival and classification of embryos in response to COLA. We observed four different reactions when cutting the cortex of worm embryos using COLA (Supplementary Fig. 2). Under the conditions we used, most of the ablation wounds quickly resealed again, and non-RNAi embryos proceeded to divide normally, which we verified by differential interference contrast imaging. Cortical resealing happened in 73% of all experiments and was typically associated with an accumulation of actomyosin at the cut site (in 203 out of 208 resealing NMY-2–GFP embryos, Supplementary Fig. 4). We observed this accumulation in both the anterior and the posterior, but detected it more easily in the anterior, in which the overall concentration of actin and myosin is higher under normal conditions. Wound healing involved both an inward-movement of the cortex from the rim of the wound towards its centre and a central accumulation of cortical material (Supplementary Fig. 4). Both processes seemed to occur simultaneously, and usually the wound resealed completely within 20–30 s post-cut. Some embryos did not reseal their wounds on the time scale on which the embryos were fluorescently monitored after COLA, but they nevertheless underwent a slightly slower, but otherwise normal, first cell division. This condition was named 'stable hole alive' and was observed only rarely (Supplementary Fig. 2). Similarly, some embryos with stable, persistent holes failed to divide ('stable hole dead'). The most

severe reaction to COLA caused the embryo to spill, probably in response to a severe puncture of the membrane.

Quantification of flow and density profiles. We used the same PIV algorithm that was used for COLA analysis to also record flow-velocity profiles along the AP axis of NMY-2–GFP-labelled zygotes. To this end, we cross-correlated two frames of 5-s interval immediately before each COLA experiment and obtained a flow field for the entire embryo at roughly 30% retraction (Fig. 4a). We omitted velocity vectors positioned outside the visible bounds of the embryo. The AP component of individual velocity vectors was averaged in each of 12 bins in an 8-μm wide stripe along the AP axis, giving an AP velocity profile. We subtracted the background fluorescence intensity of NMY-2–GFP from the same images, normalized the fluorescence intensity and averaged it along the AP axis in the same 12 bins, providing an AP NMY-2–GFP density profile. We averaged individual velocity and density profiles over 75 embryos, a subset of the embryos subjected to COLA, using two frames (with 5-s interval) immediately before laser ablation. We selected the embryos from the total set of NMY-2–GFP non-RNAi samples, using only those zygotes for which the imaged cortical plane covered more than 70% of the entire length of the embryo and which were exposed brightly enough to provide a velocity field over the entire cortex without compromising the dynamic intensity range. The resulting graph is displayed in Fig. 4b. We omitted one bin on either side owing to the larger error of PIV close to the poles, which probably arises from the local high curvature of the cortex in three-dimensions and the proximity to the embryo boundaries. We obtained the flow and density profiles for the RNAi conditions in Supplementary Fig. 10 in the same manner.

Fluorescence recovery after photobleaching (FRAP). We conducted FRAP experiments on an inverted Zeiss Axio Observer Z.1 microscope using a 63× water-immersion lens (plus 1.6× Optovar), a spinning-disk confocal head (Yokogawa), an Andor iXon EMCCD camera and an Andor FRAPPA system. We acquired the images as cortical Z-stacks of three planes at 0.5-μm spacing with an interval time of 2 s between individual stacks (iQ software, Andor Technology). We performed FRAP by bleaching a square of 12 μm × 12 μm at double repetition, with a laser dwell time of 120 μs per pixel. We monitored the recovery for a sub-square (6 μm × 6 μm) at the centre of the bleach square, and normalized it by means of the fluorescence intensity in an area of equivalent size outside the bleached area. We averaged the normalized recovery curves of several FRAP experiments and determined the characteristic recovery time by fitting the fluorescence-intensity data with an exponential function (Supplementary Fig. 10a–d).

Cytochalasin D treatment. We carried out treatment with cytochalasin D (Sigma) as described[28,45,46]. We immersed *C. elegans* zygotes at the stage of polarity establishment and polarizing flows in embryonic growth medium containing 5 μg ml^{-1} cytochalasin D, as in ref. 47. We performed imaging on an inverted Axiovert

200M microscope (Zeiss) with a 63 × water-immersion lens (C-Apochromat, NA 1.2, Zeiss), a spinning-disk confocal head (Yokogawa) and an ORCA ER camera (Hamamatsu). We acquired images in the cortical plane at 2-s intervals, and ablated the eggshell in the midplane of the embryo with the same ultraviolet laser used for COLA experiments, ablating 100 pulses at a single spot with high frequency (988 Hz). Until we permeabilized the eggshell by ultraviolet laser ablation, the embryos were protected from the drug.

31. Brenner, S. The genetics of *Caenorhabditis elegans*. *Genetics* **77,** 71–94 (1974).
32. Nance, J., Munro, E. M. & Priess, J. R. C. *elegans* PAR-3 and PAR-6 are required for apicobasal asymmetries associated with cell adhesion and gastrulation. *Development* **130,** 5339–5350 (2003).
33. Motegi, F., Velarde, N. V., Piano, F. & Sugimoto, A. Two phases of astral microtubule activity during cytokinesis in *C. elegans* embryos. *Dev. Cell* **10,** 509–520 (2006).
34. Timmons, L. & Fire, A. Specific interference by ingested dsRNA. *Nature* **395,** 854 (1998).
35. Timmons, L., Court, D. L. & Fire, A. Ingestion of bacterially expressed dsRNAs can produce specific and potent genetic interference in *Caenorhabditis elegans*. *Gene* **263,** 103–112 (2001).
36. Raffel, M., Willert, C. E., Wereley, S. T. & Kompenhans, J. *Particle Image Velocimetry: A Practical Guide.* (Springer, 2007).
37. Sveen, J. & Cowen, E. in *PIV and Water Waves: Advances in Coastal and Ocean Engineering* Vol. 9 (eds Grue, J., Liu, P. L. F. & Pedersen, G. K.) Ch 1 (World Scientific, 2004).
38. Hiramoto, Y. Rheological properties of sea urchin eggs. *Biorheology* **6,** 201–234 (1970).
39. Grill, S. W., Howard, J., Schäffer, E., Stelzer, E. H. K. & Hyman, A. A. The distribution of active force generators controls mitotic spindle position. *Science* **301,** 518–521 (2003).
40. Daniels, B. R., Masi, B. C. & Wirtz, D. Probing single-cell micromechanics *in vivo*: the microrheology of *C. elegans* developing embryos. *Biophys. J.* **90,** 4712–4719 (2006).
41. Strome, S. & Hill, D. P. Early embryogenesis in *Caenorhabditis elegans*: the cytoskeleton and spatial organization of the zygote. *Bioessays* **8,** 145–149 (1988).
42. Velarde, N., Gunsalus, K. C. & Piano, F. Diverse roles of actin in *C. elegans* early embryogenesis. *BMC Dev. Biol.* **7,** 142 (2007).
43. Gardel, M. L. *et al*. Elastic behavior of cross-linked and bundled actin networks. *Science* **304,** 1301–1305 (2004).
44. Gardel, M. L. *et al*. Stress-dependent elasticity of composite actin networks as a model for cell behavior. *Phys. Rev. Lett.* **96,** 088102 (2006).
45. Hill, D. P. & Strome, S. An analysis of the role of microfilaments in the establishment and maintenance of asymmetry in *Caenorhabditis elegans* zygotes. *Dev. Biol.* **125,** 75–84 (1988).
46. Hyman, A. A. & White, J. G. Determination of cell division axes in the early embryogenesis of *Caenorhabditis elegans*. *J. Cell Biol.* **105,** 2123–2135 (1987).
47. Shelton, C. A. & Bowerman, B. Time-dependent responses to *glp-1*-mediated inductions in early *C. elegans* embryos. *Development* **122,** 2043–2050 (1996).